Rare Metal Materials and Engineering

Available online at **www.rmme.ac.cn**

Cite this article as: Rare Metal Materials and Engineering,

DOI: https://doi.org/10.12442/j.issn.1002-185X.20250402.

The influence of thermomechanical processing on the microstructure and mechanical properties of NiCo-based superalloys

Gao Ming [1], **Zhang Qian** [1], **Qiao Junwei** [1, 2], **Gan Bin** [3]

[1] College of Materials Science and Engineering, Taiyuan University of Technology, Taiyuan 030024, China; [2] Key Laboratory of Interface Science and Engineering in Advanced Materials, Ministry of Education, Taiyuan University of Technology, Taiyuan 030024, China; [3] Suzhou Laboratory, No. 388, Ruoshui Street, Suzhou, Jiangsu 215123, China

Abstract: Achieving an optimal strength-ductility synergy efficiently is a critical objective for advanced structural materials. This study developed a novel grain structure in a NiCo-based superalloy, consisting of residual deformed grains, fine recrystallized grains, and multi-scale L12-γ′ precipitates, using a short-term annealing and aging treatment. Compared to the conventional heat-treated condition (yield strength: 1,106 MPa; elongation: 18.8%), the alloy with a partially recrystallized microstructure exhibited a significantly higher yield strength of 1,371 MPa, while maintaining a ductility of 13.3%. This high strength is attributed to synergistic effects from dislocation strengthening (induced by prior cold rolling), fine grain strengthening, and precipitation reinforcement by γ′ phases. In contrast, the fully recrystallized variant demonstrated a yield strength of 1,390 MPa with an elongation of 14.3%, primarily due to a uniform fine-grained structure and homogeneous γ′ precipitation. The underlying deformation mechanisms were thoroughly investigated, revealing that dislocation activity, nano-twins, and L-C locks, in addition to the precipitates, are critical for the outstanding mechanical properties. This work provides a practical and cost-effective processing strategy for developing high-performance NiCo-based superalloys for demanding engineering applications.

Key words: NiCo-based superalloy; Thermo-mechanical treatment; Strength-ductility synergy; $L1_2$-γ′ precipitation; Microstructure evolution

稀有金属材料与工程

1 Introduction

Nickel-based superalloys are a prominent class of alloys recognized for their exceptional tensile strength, corrosion resistance, fatigue resistance, creep strength, and superior workability. These properties are predominantly influenced by the thermomechanical processing employed, rendering them highly applicable in fields such as aerospace, petrochemicals, chemical engineering, and nuclear industries [1-3]. Achieving high strength and ductility has remained a critical objective in current research [4,5]. However, most superalloys typically encounter the strength-ductility trade-off dilemma [6]. Typically, strengthening strategies such as solid solution hardening [7,8], grain refinement hardening [9,10], and precipitation hardening [11,12] are employed to improve the mechanical properties of superalloys. Various internal defects, including solute atoms, grain

---

Foundation item: Basic Research Program of Jiangsu (No. BK20240021)

Corresponding author: Qiao Junwei, Ph.D., Professor, Key Laboratory of Interface Science and Engineering in Advanced Materials, Ministry of Education, Taiyuan University of Technology, Taiyuan 030024, China, E-mail: qiaojunwei@gmail.com; Gan Bin, Ph.D., Professor, Suzhou Laboratory，No. 388，Ruoshui Street, Suzhou, Jiangsu 215123, China, E-mail: ganb@szlab.ac.cn

Copyright © 2025, Northwest Institute for Nonferrous Metal Research. Published by Science Press. All rights reserved.

boundaries, and precipitates, can impede dislocation motion, thereby contributing to enhanced strength [13,14]. Nevertheless, due to strain localization [15,16], these strengthening strategies often significantly compromise the ductility of superalloys, thereby increasing safety risks. Given the limitations of the aforementioned methods, superalloys necessitate an alternative strengthening strategy. In recent years, the concept of 'material planarization' has been introduced, presenting a novel strategy for improving the mechanical properties of metals and their alloys [17,18]. This strategy coordinates various properties of alloys by controlling stable microstructures at different length scales, with minimal or no alterations to the material composition [19].

Researchers demonstrate that gradient structures and grain refinement are key strategies to enhance the strength-ductility balance in metals [20,21]. Thermomechanical processing effectively tailors microstructures and mechanical properties [22,23]. For instance, Polkowska et al. [6] cold-rolled and heat-treated Haynes® 282® alloy (low SFE) at 10–70% deformation, observing increased yield strength but reduced elongation. Gu et al. [24] used torsional deformation and aging to create gradient structures, improving ductility over cold drawing but weakening strength. Zeng et al. [25] combined cryogenic rolling (reducing SFE to form nanoscale twins) with recrystallization annealing, achieving grain refinement and enhanced ductility at the expense of strength. This highlights the limitations of relying solely on grain refinement. To address this, Wang et al. [26] incorporated γ′ precipitates into fine-grained structures, boosting strength without sacrificing ductility. Similarly, Chen et al. [27] applied short-term heat treatment and aging to cold-drawn GH159 superalloy, where heterogeneous deformation and multi-scale $L1_2$-γ' precipitates induced HDI strengthening, enabling exceptional strength-ductility synergy. Furthermore, severe plastic deformation methods, including equal-channel angular pressing (ECAP), high-pressure torsion (HPT), and accumulative roll bonding (ARB), are also incorporated into thermomechanical processes, enabling further ultimate control over the microstructure of alloys. These studies emphasize that combining multiple approaches—such as gradient structures, refined grains, and precipitates—overcomes the trade-off between strength and ductility. Thermomechanical methods and microstructural engineering collectively enable tailored properties, demonstrating the importance of hybrid strategies in advanced alloy design. Zhang et al. [28] proposed that NiCoCr alloys have a low stacking fault energy (SFE) and a high tendency to form nanotwins. These characteristics hinder dislocation motion and adapt to plastic deformation to achieve high strength and ductility. Therefore, a new type of nickel-cobalt-based superalloy was designed based on low SFE, which is prone to twinning due to cross-slip inhibition during plastic deformation [29].The increase of Co content in the superalloy reduces the initial γ' dissolution temperature and increases the heat treatment temperature range.

Building on this foundation, this study employs a novel NiCo-based superalloy as a model system to systematically investigate the evolution of grain size and γ' precipitates under combined cold rolling and annealing processes. A quantitative assessment of the contributions from distinct strengthening mechanisms is conducted, coupled with an in-depth analysis of the microstructural evolution during alloy deformation. The study aims to elucidate the synergistic strengthening and plasticizing mechanisms arising from ultrafine-grained structures and multi-scale γ' precipitates, thereby establishing theoretical frameworks and technical guidelines for designing high-performance Ni-based superalloys. The research prioritizes the precise control of thermomechanical processing to achieve nanoscale $L1_2$-structured γ' precipitates with high density and uniform dispersion, while retaining a micrometer-scale gradient grain architecture. This approach overcomes the performance limitations of conventional superalloys, enabling concurrent improvements in strength and ductility. These advancements offer robust material solutions for critical applications such as aerospace, driving technological progress in high-temperature structural materials.

2 Materials and methods

2.1 Specimen preparation

The chemical composition of the novel nickel-based superalloy was presented in Table 1. The superalloy ingot was prepared using a triple-melting process, which included vacuum induction melting (VIM), protective atmosphere electroslag remelting (ESR), and vacuum arc remelting (VAR). Following high-temperature homogenization treatment, the alloy ingot was forged into a rod with dimensions of φ150 × 360 mm. Axial specimens were extracted from the 1/2 R position of the forged alloy rod. The forged samples underwent standard heat treatment. Solution treatment was performed at 1,080 ℃ for 2 hours, followed by air cooling to room temperature. Subsequently, a two-stage aging treatment (650 ℃/24h/AC and 760 ℃/16h/AC) was carried out to obtain the standard heat-treated alloy sample (ST).

According to Figure S1, the solid solution temperature of the selected area in this paper is 1080 ℃, which is the sub-solid solution temperature. After the solid solution treatment, the primary γ′ is retained, and the secondary and tertiary γ′ are completely dissolved. It is mainly to construct a multi-size gradient γ′ phase and inhibit the growth of recrystallized grains in the later stage. The reasons for choosing 650 ℃ and 760 ℃ as the aging temperature are as follows: in the first stage, the lower aging temperature of 650 ℃ can promote the formation of a large number of small and dispersed γ′ phases. In the second stage, the high temperature aging at 760 ℃ is mainly aimed at spheroidizing γ′ precipitates and coarsening to the appropriate size, so as to achieve a good balance between strength and plasticity. Due to the uniform precipitation of the secondary γ′ phase in the previous step, there are few γ′ phase forming elements left in the matrix, which makes the tertiary γ′ phase only precipitate around the secondary γ′ phase, and the volume fraction of the $L1_2$ precipitation phase at the current temperature tends to be stable.

Table 1 Chemical composition of Ni-Co based superalloy (wt %)

Co	Cr	W	Al	Ti	Nb	C	Ni
20	16.5	5.0	2.5	2.5	2.5	0.02	Bal.

2.2 Thermomechanical Processing

Thermomechanical processing (TMP) was conducted on the forged samples between solution treatment and aging. The solution-treated samples were cold-rolled at room temperature using a twin-roll cold rolling mill to achieve a deformation of 70% (without surface cracks). Subsequently, the samples were annealed at 1025 °C, 1050 °C, and 1075 °C for varying durations, followed by a two-stage aging treatment at 650 °C/24 h/AC and 760 °C/16 h/AC. During thermomechanical processing, annealing and recrystallization were employed to control the grain size, morphology, and distribution of precipitates in the novel nickel-based superalloy. Additionally, the substructures were introduced into the unrecrystallized regions to mitigate dislocation pile-up at grain boundaries. The specific parameters and designations were provided in Table 2.

Table 2 Different heat treatment schedules and names of samples

Treatment method	Samples
Solution treatment＋two-stage aging treatment	ST
Solution treatment＋cold rolling + annealing at 1,298 K for 15min＋two-stage aging treatment	1,025-15
Solution treatment＋cold rolling + annealing at 1,298 K for 30min＋two-stage aging treatment	1,025-30
Solution treatment＋cold rolling + annealing at 1,298 K for 60min＋two-stage aging treatment	1,025-60
Solution treatment＋cold rolling + annealing at 1,325 K for 15min＋two-stage aging treatment	1,050-15
Solution treatment＋cold rolling + annealing at 1,325 K for 30min＋two-stage aging treatment	1,050-30
Solution treatment＋cold rolling + annealing at 1,325 K for 60min＋two-stage aging treatment	1,050-60
Solution treatment＋cold rolling + annealing at 1,348 K for 15min＋two-stage aging treatment	1,075-15
Solution treatment＋cold rolling + annealing at 1,348 K for 30min＋two-stage aging treatment	1,075-30
Solution treatment＋cold rolling + annealing at 1,348 K for 60min＋two-stage aging treatment	1,075-60

2.3 Mechanical testing

Uniaxial tensile tests were performed at room temperature using a universal testing machine (Instron 5969) with a constant loading rate of 3×10^{-4} s^{-1}. Dog-bone-shaped tensile specimens were machined from samples in various states, with a gauge section measuring 10 mm in length and 3.0 mm in width. The tensile direction was oriented along the rolling direction. To ensured repeatability and accuracy, three tensile tests were performed for each processing condition.

2.4 Microstructure characterization

The microstructure of the samples was characterized using X-ray diffraction (XRD), electron backscatter diffraction (EBSD), scanning electron microscopy (SEM), transmission electron microscopy (TEM), and selected area electron diffraction (SAED). XRD characterization of the samples in various states was performed using the Philips APD-10D diffractometer, with Cu-Kα radiation as the source and a scanning angle range of 20° to 120°. Additionally, the Phenom XL scanning electron microscope (SEM) was utilized to characterize the microstructure of electrochemically polished samples. For grain structure observation, the samples were electrolytically polished using a reagent composed of 20% H_2SO_4 + 80% CH_3OH. Electrolytic polishing was performed using a dedicated power supply, with a voltage of 15-25 V, at room temperature, and a polishing time of 5-8 s. For precipitate observation, the samples were subjected to electrolytic etching after polishing, using a reagent composed of 15 g Cr_2O_3, 10 ml H_2SO_4, and 150 ml H_3PO_4. Electrolytic etching was conducted at a voltage of 4.5 V, at room temperature, for 4-8 s. Prior to EBSD analysis, the samples were electrolytically polished using the same reagent (20% H_2SO_4 + 80% CH_3OH) with a voltage of 15-25 V, at room temperature, and a polishing time of 5-8 s. The texture structure of the samples was analyzed using an EBSD system equipped with a JSM-IT700HR field-emission scanning electron microscope, with a step size of 0.25 μm and an accelerating voltage of 20 kV. The post-tensile samples were characterized using a spherical aberration-corrected 200 kV JEM-ARM300F2 transmission electron microscope (TEM). The samples were first mechanically ground to a thickness of less than 50 μm, then punched into 3-mm diameter discs. Finally, the discs were thinned to electron transparency using a twin-jet electropolisher with the same solvent used for electrochemical polishing, at a DC voltage of 20 V and a temperature of approximately -10 °C. The size and distribution of precipitates were statistically analyzed using Image J.

3 Results

3.1 Microstructure evolution

Fig.1(a-c) presents SEM images of the samples in different processing states. As illustrated in Fig. 1(a), the as-forged microstructure of the NiCo-based superalloy consists of a mixed grain structure, comprising equiaxed grains with a size of approximately 74 μm and fine grains with a size smaller than 2-4 μm. The fine grains are uniformly distributed surrounding the equiaxed grains. Fig.1(b) shows the microstructure after solution treatment of as-forged NiCo-based superalloy at 1,080 °C, in which the mixed grain structure recrystallized completely, resulting in a uniformly distributed equiaxed grain structure with a consistent grain size. Fig.1(c) illustrates the microstructure after standard heat treatment. It is that an abundance of equiaxed grains is found. Fig.1(d) presents a high-magnification image of

稀有金属材料与工程

the γ′ precipitate distribution under the standard heat-treated state, revealing uniformly distributed spherical γ′ precipitates. Measurements using Image Pro Plus indicate that the average size of the γ′ precipitates is 25.7 ± 2.0 nm, with a volume fraction of 40.3 ± 1.1%. These γ′ phases hinder dislocation movement, thereby enhancing the strength of the Nickel-based superalloy [30].It can be concluded that after solution treatment and two-stage aging, the as-forged NiCo-based superalloy achieves an initial alloy with uniformly distributed grains and consistent-sized precipitates. The mechanical properties of this initial alloy exhibit greater stability, serving as a benchmark for comparison and providing a reliable material foundation for subsequent thermomechanical processing.

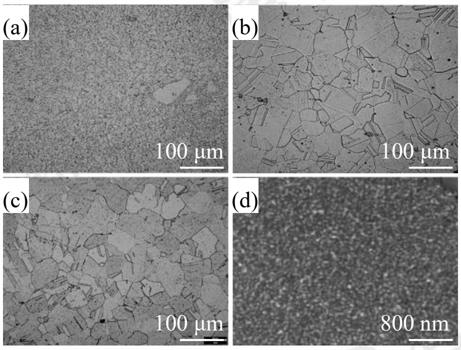

Fig.1 Microstructures of the alloy in different states: (a) As-forged alloy; (b) Solution-treated alloy; (c) Alloy after standard heat treatment; (d) Microstructure of γ′ phase

3.2 Microstructural evolution during thermomechanical processing

The XRD patterns of the samples in various states after thermomechanical processing are presented in Fig. 2. From the XRD patterns, it is evident that the alloys treated at different annealing temperatures and times exhibit a distinct FCC structure, with prominent diffraction peaks at approximately 51.3°, 59.9°, and 89.9° in 2θ, corresponding to the (111), (200), and (220) planes, respectively. A distinct double peak is seen at 89.9°, which can be deconvoluted to separate the γ′ precipitate phase from the γ matrix. Furthermore, as the annealing time increases and the temperature rises, the peak intensity of the γ′ precipitates gradually decreases. This may be attributed to variations in the content and size of the precipitates under different thermomechanical processing conditions.

Fig.3 presents SEM images of nine samples subjected to different thermomechanical processing conditions. Fig.3 (a-c) display the microstructures of samples annealed at 1,025 °C, all of which exhibit an incompletely recrystallized structure consisting of recrystallized and deformed regions. Prolonged annealing drives the progressive transformation of deformed grains into fine recrystallized grains, accompanied by the presence of coarse primary γ′ precipitates distributed both within grain interiors and along grain boundaries. Fig. 3(d-f) illustrate the microstructures of samples annealed at 1,050 °C, exhibiting a fully recrystallized structure with randomly oriented equiaxed grains. With prolonged annealing durations, coarse γ′ precipitates become predominantly localized at grain boundaries. The Zener pinning effect exerted by these precipitates results in moderate grain coarsening, with average grain size increasing from 3.8 μm after 15 minutes to 4.6 μm following 60 minutes of annealing. Fig. 3(g-i) present the microstructures of samples annealed at 1,075 °C, exhibiting a clearly recrystallized structure with significantly coarsened grains and a large number of annealing twins. As the annealing time increases, the grain size increases from 8.6 μm at 15 min to 12.0 μm at 60 min. Previous studies have shown that the grain structure changes with annealing temperature, indicating that the grain size increases progressively as the annealing temperature rises [31]. When the temperature exceeds the solvus temperature of the γ′ precipitates, the pinning force of the particles is eliminated, resulting in abnormal grain growth behavior [13,32].

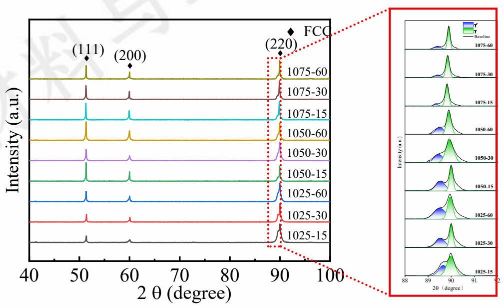

Fig.2 XRD patterns of different states after thermomechanical treatment

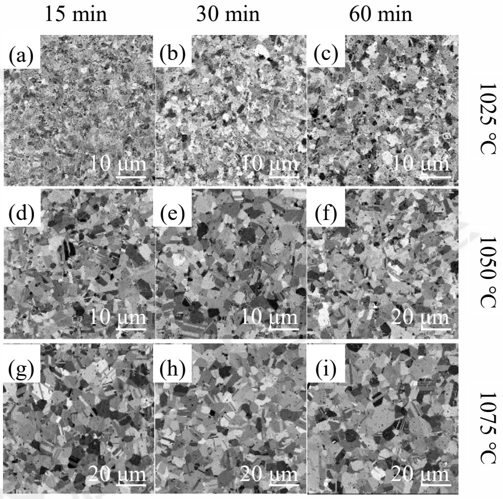

Fig.3 SEM images of the grain morphology in samples subjected to different thermomechanical treatments: (a-c) 1,025-(15,30,60); (d-f) 1,050-(15,30,60); (g-i) 1,075-(15,30,60)

Fig.4 presents SEM images of the γ′ precipitates in nine samples subjected to different thermomechanical processing conditions. Fig.4(a-c) correspond to the 1025-(15, 30, 60) samples. In the samples annealed at 1,025 °C, primary, secondary, and tertiary γ′ precipitates are found. The irregularly shaped large particles are primary precipitates, while the secondary precipitates—mostly spherical, rod-like, or butterfly-shaped—are primarily distributed in the recrystallized regions, driven by the internal

稀有金属材料与工程

stress from the deformed structure[33]. Uniformly distributed spherical tertiary precipitates are located between the primary and secondary precipitates. Fig.4(d-f) correspond to the 1,050-(15, 30, 60) samples. In the samples annealed at 1,050 °C, primary, secondary, and tertiary γ' precipitates are present. The irregularly shaped large particles are primary precipitates, while the spherical or near-spherical secondary precipitates are uniformly distributed within the matrix. Uniformly distributed spherical tertiary precipitates are located between the primary and secondary precipitates. Fig.4(g-i) correspond to the 1,075-(15, 30, 60) samples. In the samples annealed at 1,075 °C, primary and tertiary γ' precipitates are present. The irregularly shaped large particles are primary precipitates, while the spherical tertiary precipitates are uniformly distributed within the matrix.

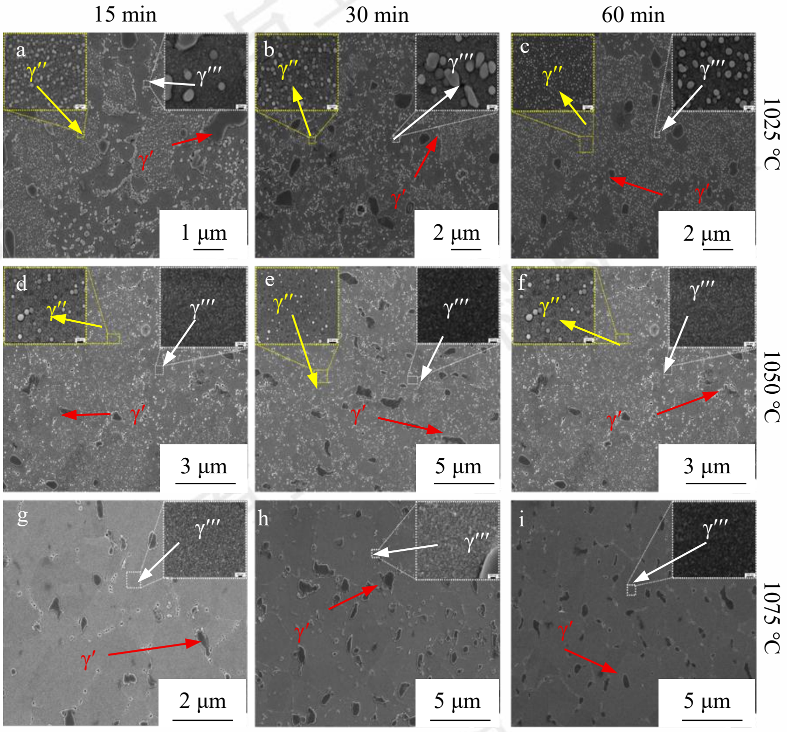

Fig.4 SEM images of the γ' phase in samples under different thermomechanical treatments: (a-c) 1,025-(15,30,60); (d-f) 1,050-(15,30,60); (g-i) 1,075-(15,30,60)

For the partially recrystallized samples (1,025-(15, 30, 60)), as the annealing time increases, the primary γ' particles become more regular, and the sharp corners begin to dissolve (Fig.4(c-d)). For the fully recrystallized samples (1,050-(15, 30, 60)), the sharp corners completely dissolve, and the morphology of the secondary γ' precipitates gradually transforms from irregular spheres to spherical shapes (Fig.4(e-f)). The morphology of the tertiary γ' particles does not change significantly with annealing temperature and remains spherical. Additionally, as the annealing temperature increases, the average size of the secondary γ' particles continues to increase, while their number decreases. Both the average size and number of the tertiary γ' particles gradually increase. This indicates that as the degree of recrystallization increases, the precipitation of tertiary γ' particles tends to become finer and more uniform, while the nucleation sites for secondary γ' particles decrease. This is because, as recrystallization progresses, the stress concentration induced by the rolling process is gradually released, reducing the driving force for elemental diffusion and the number of nucleation sites, thus blocking the pathways for rapid growth of large γ' particles. Simultaneously, to maintain the system's low surface energy, the γ' particles tend to precipitate in a spherical shape and grow uniformly with minimal surface energy[34].

Table 3 presents the volume fractions of primary, secondary, and tertiary γ' precipitates in samples under various conditions. It is found that as the annealing temperature increases and the annealing time extends, the volume fraction of secondary γ' precipitates gradually decreases and completely dissolves at 1075 °C, while the volume fraction of tertiary γ' precipitates increases. The volume fraction of primary γ' precipitates remains relatively constant. For all samples under various conditions, the total volume fraction of precipitates ranges between 38% and 40%. Table 4 provides the statistical data on the sizes of primary, secondary, and tertiary γ' precipitates in samples under various conditions. It is concluded that the annealing temperature and time have little effect on the sizes of primary and tertiary γ' precipitates. However, as the annealing temperature increases and the annealing time extends, the size of secondary γ' precipitates increases. An optimal precipitate density effectively impedes dislocation motion, thereby enhancing strength and hardness. However, excessive precipitates induce stress concentration at interfaces, leading to reduced fracture

稀有金属材料与工程

toughness. Notably, nanoscale precipitates generate intensified stress fields due to their high interfacial strain energy, which impose stronger barriers to dislocation glide and further amplify the strengthening effect.

Table 3 Volume fractions of primary, secondary, and tertiary γ′ precipitate phases in samples under different conditions

	1,025-15	1,025-30	1,025-60	1,050-15	1,050-30	1,050-60	1,075-15	1,075-30	1,075-60
Primary γ′ (%)	4.7±0.2	4.8±0.2	4.5±0.3	4.7±0.5	5.0±0.1	4.4±0.4	3.9±0.2	4.4±0.2	4.4±0.3
Secondary γ′ (%)	25.0±2.4	20.3±3.2	16.2±3.4	13.2±4.2	7.2±2.1	8.1±2.8	0	0	0
Tertiary γ′ (%)	13.0±1.4	14.3±2.4	19.1±3.2	20.7±2.7	29.3±3.9	25.5±3.4	36.1±2.5	36.2±3.8	36.1±3.1

Table 4 Sizes of primary, secondary, and tertiary γ′ precipitate phases in samples under different conditions

Diameter	1,025-15	1,025-30	1,025-60	1,050-15	1,050-30	1,050-60	1,075-15	1,075-30	1,075-60
Primary γ′ (μm)	2.1±0.4	2.1±0.3	2.2±0.3	2.2±0.4	2.9±0.3	2.4±0.4	2.5±0.5	2.6±0.4	2.7±0.5
Secondary γ′ (nm)	48.3±9.2	52.3±10.8	77.5±15.1	72.6±15.7	69.5±15.4	79.2±15.8	0	0	0
Tertiary γ′ (nm)	9.7±2.1	9.6±2.2	9.7±1.8	9.5±2.3	10.2±2.0	10.1±1.6	9.7±2.0	9.5±1.2	10.0±2.1

Fig. 5 presents the EBSD images of the ST sample, as well as the 1,025-15, 1,050-15, and 1,075-15 samples. Fig. 5(a_1-a_4) display the inverse pole figure (IPF) maps for the samples under different conditions. The grains in the ST sample are randomly oriented equiaxed grains, with annealing twins detected in some of them. The 1,025-15 sample shows an incompletely recrystallized structure, with a noticeable strain gradient in the medium-axis grains. Both the 1,050-15 and 1,075-15 samples are fully recrystallized, featuring randomly oriented equiaxed grains. It is evident that the degree of recrystallization is highly dependent on the annealing temperature, with complete recrystallization occurring when the annealing temperature exceeds 1,050 °C.

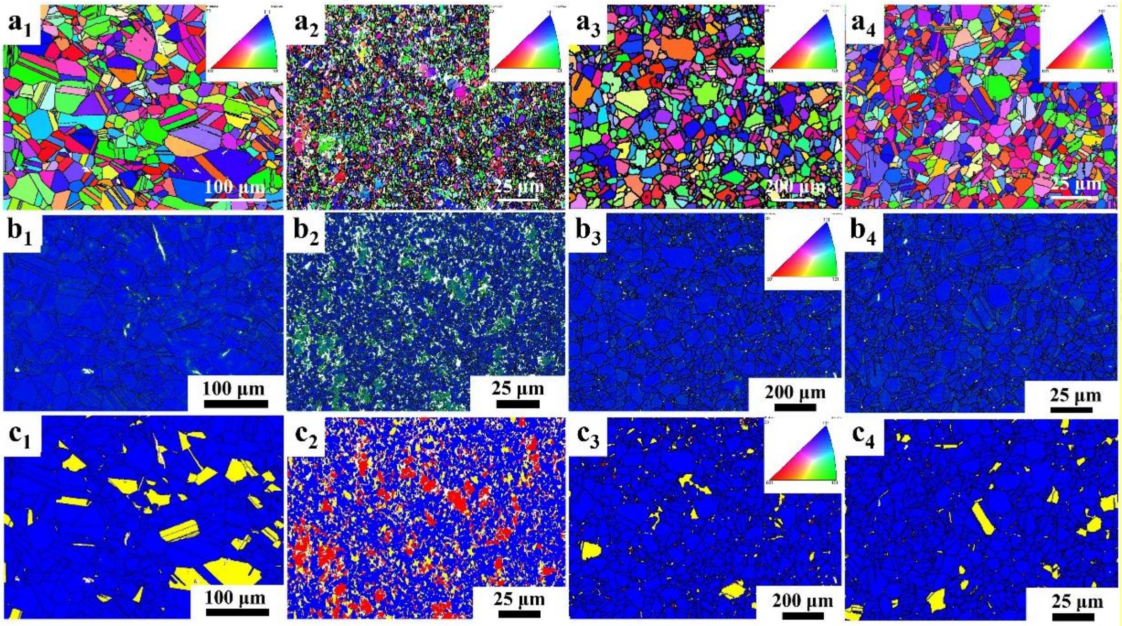

Fig.5 EBSD analysis of ST specimens and specimens 1,025-15、1,050-15、1,075-15: (a_1-a_4) IPF maps; (b_1-b_4) KAM maps; (c_1-c_4) Recrystallization distribution maps

Fig. 5(b_1-b_4) show the kernel average misorientation (KAM) maps for the samples under different conditions. The KAM distribution characterizes local misorientation, helping to determine the geometrically necessary dislocation density in different grains [35]. The ST sample exhibits no stress concentration at the grain boundaries. In contrast, significant stress concentration is detected at the grain boundaries and within the grains of the 1,025-15 sample, while the 1,050-15 and 1,075-15 samples show no noticeable stress concentration. Figs. 5(c_1-c_4) present the recrystallization maps for the samples under different conditions. The grains in the ST sample are primarily recrystallized, with a small fraction of subgrains. About 27% of the deformed grains are found in the medium-axis grains of the 1,025-15 sample. In the 1,050-15 and 1,075-15 samples, all grains are fully recrystallized. The EBSD analysis confirms that during thermomechanical processing, the 1,050-15 sample is at the critical point of complete recrystallization, consisting entirely of fully recrystallized structures, with no significant stress concentration or deformed grains.

Fig.6 illustrates the grain boundary types and misorientation distribution maps for the ST sample, along with the 1,025-15, 1,050-15, and 1,075-15 samples. Based on the misorientation angle, the grain boundaries are classified into subgrain boundaries (θ<2°), low-angle grain boundaries (2°<θ<15°), high-angle grain boundaries (θ>15°), and annealing twin boundaries (θ=60°; Σ3). The proportions of each type of grain boundary in the samples under different conditions are provided in Table 5. As the annealing temperature increases, the proportion of subgrain boundaries decreases significantly; the proportion of low-angle grain boundaries decreases gradually; the proportion of high-angle grain boundaries increases sharply; and the proportion of annealing twin boundaries increases progressively. It is evident that the grain boundary characteristics and misorientation distribution of the NCo-based superalloy are influenced by the annealing treatment. The standard heat-treated alloy predominantly consists of high-angle grain boundaries, with nearly 50% consisting of annealing twin boundaries. Furthermore, as the degree of recrystallization increases, the strain at the grain boundaries decreases progressively, and the length of subgrain boundaries and low-angle grain boundaries reduces gradually. Due to the influence of temperature, the length of annealing twin boundaries increases gradually, resulting in an increase in the proportion of annealing twin boundaries.

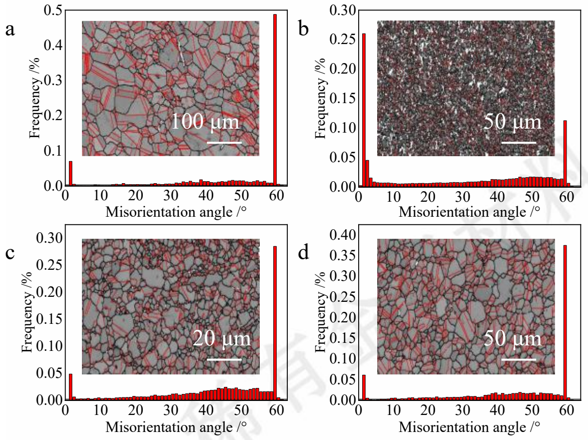

Fig.6 Grain boundary orientation difference maps of samples in different states: (a)ST；(b)1,025-15；(c)1,050-15；(d)1,075-15

Table 5 Proportion of various grain boundaries in samples in different states

Samples	Sub-structures /%	LAGBs /%	HAGBs /%	Annealing TBs/%
ST	7.1	2.6	90.3	48.8
1,025-15	26.2	13.3	60.5	11.3
1,050-15	4.9	4.7	90.4	28.5
1,075-15	6.2	4.5	89.3	37.5

3.3 Mechanical properties

Fig.7(a) illustrates the typical tensile engineering stress-strain curves for the samples under different conditions, Fig. 7(b) shows the bar charts of the tensile properties of each specimen at 25 °C. In this study, after thermomechanical processing, the Ni-based superalloy samples annealed at 1,025 °C and 1,050 °C exhibited an increase in both yield strength and ultimate tensile strength, accompanied by a gradual decrease in elongation. In contrast, the samples annealed at 1,075 °C exhibited a decrease in both yield strength and ultimate tensile strength, with elongation also progressively decreasing as the annealing time increased. The yield strength of the standard heat-treated alloy at 25 °C is 1,106 MPa. After thermomechanical processing, the 1,025-15 sample achieved a yield strength of 1,371 MPa at 25 °C, representing an increase of approximately 26.2% compared to the standard heat-treated alloy. As the annealing temperature increased, the 1,050-15 sample reached a yield strength of 1,390 MPa at 25 °C, an improvement of approximately 24% over the standard heat-treated alloy. However, the 1,075-15 sample exhibited a yield strength of 954 MPa at 25 °C, reflecting a decrease of approximately 14% compared to the standard heat-treated alloy. Correspondingly, the elongation of the 1,025-15 and 1,050-15 samples decreased from 18.8% to 13.3% and 14.3%, respectively, while the elongation of the 1,075-15 sample increased to 22.9%.

Fig. 7(c) illustrates the Vickers hardness of the Ni-based superalloy under different conditions. The hardness of the ST sample is 494 HV. After thermomechanical processing, the hardness of the samples increases significantly. The hardness of the 1,025-15 sample reaches 555 HV, while that of the 1,050-15 sample increases to 547 HV. In the 1,075-(15,30,60) samples, as recrystallization is nearly complete and the stored dislocation density in the alloy is relatively low, the hardness values exhibit minimal variation and remain relatively low. As the annealing temperature increases and the annealing time extends, dislocations are eliminated more slowly below the recrystallization temperature, resulting in partial dislocation entanglement and pile-up in the alloy. During the subsequent aging process, the lower temperature cannot effectively eliminate the work hardening caused by the high dislocation density, leading to a notable increase in sample hardness. Above the recrystallization temperature, the hardness of the alloy stabilizes, approaching that of the standard heat-treated alloy

4 Discussions

4.1 Strengthening mechanisms

For the novel Ni-based superalloy studied in this experiment, the contribution to yield strength arises from lattice intrinsic strength (σ_0), solid solution strengthening (σ_s), grain boundary strengthening (σ_g), precipitation strengthening (σ_p), and dislo-

稀有金属材料与工程

cation strengthening (σ_d). The specific relationship can be expressed as:

$$\sigma_y = \sigma_0 + \sigma_s + \sigma_g + \sigma_p + \sigma_d \tag{1}$$

The following discussion primarily focuses on the contributions of grain boundary strengthening (σ_g), precipitation strengthening (σ_p), and dislocation strengthening (σ_d) to the mechanical properties of the alloy at room temperature.

4.1.1 Grain boundary strengthening

The introduction of grains with varying sizes via cold rolling and subsequent annealing treatments results in a significant strengthening of these samples. The Hall-Petch relationship defines the influence of grain boundary strengthening[36,37]:

$$\sigma_g = k_y {d_0}^{\left(-\frac{1}{2}\right)} \tag{2}$$

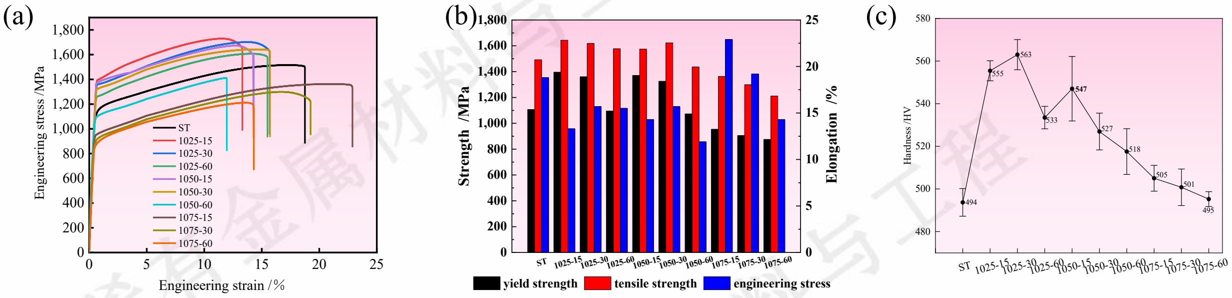

Fig. 7 Mechanical behaviors of the new nickel-based superalloy under different processes: (a) Engineering stress-strain curves; (b) Column chart of mechanical properties; (c) Vickers hardness

where k_y is the Hall-Petch coefficient, approximately 750 MPa μm$^{1/2}$ for pure nickel and various superalloys[13], and the average grain size (d_0) are key parameters in this analysis. For the 1,025-(15, 30, 60) specimens, which were in a partially recrystallized state, the grain boundary strengthening contribution was calculated using the modified strength formula $\sigma_g = k_y d_0$^$(-1/2) f_{RX}$, where f_{RX} represents the volume fraction of recrystallized regions determined by EBSD analysis. The calculated yield strength increments from grain boundary strengthening were approximately 278 MPa, 298 MPa, and 341 MPa for these specimens. For the 1,050-(15, 30, 60) and 1,075-(15, 30, 60) specimen series, the corresponding increments were approximately 255 MPa, 231 MPa, 216 MPa, 198 MPa, 186 MPa, and 167 MPa, respectively. Notably, the grain boundary strengthening contributions were significantly higher for the 1,025-(15, 30, 60) and 1,050-(15, 30, 60) specimens compared to the 1,075-(15, 30, 60) series. This observation suggests that increasing annealing temperature and duration leads to grain coarsening, consequently reducing the strengthening effect from grain boundaries. Compared to alloys with similar compositions, the present processing technique demonstrates remarkable grain refinement strengthening effects [38].

4.1.2 Precipitation strengthening

Considering the characteristics of the precipitates, the interaction between precipitates and dislocations can occur via two mechanisms: cutting or bypassing (Orowan looping). The primary γ' particles, which are larger, primarily interact with dislocations via the bypassing mechanism, while the secondary and tertiary γ' precipitates, being smaller, predominantly interact via the cutting mechanism. This critical size is usually about 100 nm [39].

When dislocations bypass precipitates via Orowan looping, the critical stress σ_{or} can be described by the classical equation [40,41]:

$$\Delta\sigma_{or} = M \frac{0.4Gb}{\pi\sqrt{1-\upsilon}} \frac{\ln\left(\frac{2r_m}{b}\right)}{\lambda_p} \tag{3}$$

where M=3 is the Taylor factor, G=81.4 GPa is the shear modulus, v=0.31 is Poisson's ratio (as referenced in prior studies [42]), and b is the Burgers vector. For FCC structures, b=$\sqrt{2/2} \times a_{\mathrm{Ti2Al4}} = 0.253\ \mathrm{nm}$. $\bar{r}$=$\sqrt{2/3} \cdot r$ is the average particle radius on the slip plane, where r represents the average particle radius. $L_p = 2\bar{r}\left(\sqrt{\frac{\pi}{4f}} - 1\right)$ is the average interparticle distance, where f is the volume fraction of the precipitate phase. Taking the 1050-15 specimen as an example, the primary γ' precipitates reached micrometer-scale dimensions, leading to predominant dislocation interaction through the bypassing mechanism. As shown in Table 3 and Table 4, the average precipitate radius on the slip plane was measured as 1.8 μm with an average interparticle spacing of 9.4 μm. The $\Delta\sigma_{or}$ for the 1050-15 specimen was determined to be 9.6 MPa, which can be attributed to the large size and low volume fraction of the primary γ' precipitates. Consequently, the bypassing mechanism does not play a dominant role in precipitation strengthening for this specimen.

When dislocations shear through precipitates, the primary strengthening contributions arise from coherency strengthening ($\Delta\sigma_{cs}$), modulus strengthening ($\Delta\sigma_{ms}$), and order strengthening ($\Delta\sigma_{os}$) mechanisms [43]. Notably, coherency strengthening and modulus strengthening become effective before dislocation cutting occurs, while order strengthening operates during the shearing process. The overall precipitation strengthening

稀有金属材料与工程

contribution is determined by comparing the sum of coherency and modulus strengthening ($\Delta\sigma_{cs} + \Delta\sigma_{ms}$) with order strengthening, with the larger value representing the dominant mechanism.

$$\Delta\sigma_{\mathrm{cs}} = M \cdot \alpha_{\varepsilon}(G \cdot \varepsilon_c)^{\frac{3}{2}}\left(\frac{rf}{0.5Gb}\right)^{\frac{1}{2}} \tag{4}$$

$$\Delta\sigma_{ms} = 0.0055M(\Delta G)^{\frac{3}{2}}\left(\frac{2f}{G}\right)^{\frac{1}{2}}\left(\frac{r}{b}\right)^{\frac{3m}{2}-1} \tag{5}$$

$$\Delta\sigma_{os} = 0.81M\frac{\gamma_{APB}}{2b}\left(\frac{3\pi f}{8}\right)^{\frac{1}{2}} \tag{6}$$

here, α_{ε}=2.6 is a constant, ε_c=0.002 represents the constrained lattice misfit strain, and *r* and *f* denote the average radius and volume fraction of the precipitates, respectively. Additionally, ΔG=81.4-77.4 =4 GPa (where G_{L12} = 77.4 GPa, taken from $\mathrm{Ni_3(Al, Ti)}$[44]), m=0.85 is a constant, and γ_{APB}= 21.8 mJ/m^2 is the antiphase boundary energy (APBE) of the precipitates. Taking the 1050-15 specimen as an example, we systematically analyzed the strengthening contributions from γ′ precipitates with different size distributions. For the tertiary γ′ precipitates (volume fraction: 20.70%, average size: 9.5 nm), the calculated strengthening contributions were approximately 223 MPa from coherency strengthening ($\Delta\sigma_{cs}$), 25 MPa from modulus strengthening ($\Delta\sigma_{ms}$), and 52 MPa from order strengthening ($\Delta\sigma_{os}$). Previous studies on γ + γ′ high-entropy alloys have demonstrated that order strengthening becomes dominant when γ′ precipitate sizes are below 25-35 nm[42]. However, in the present study, the relatively low antiphase boundary energy of the precipitates resulted in diminished order strengthening effects. By comparing ($\Delta\sigma_{cs} + \Delta\sigma_{ms}$) with $\Delta\sigma_{os}$, the total precipitation strengthening ($\Delta\sigma_p$) from tertiary γ′ was determined to be 249 MPa. For the secondary γ′ precipitates (volume fraction: 13.20%, average size: 72.57 nm), the corresponding strengthening contributions were 494 MPa ($\Delta\sigma_{cs}$), 1 MPa ($\Delta\sigma_{ms}$), and 41 MPa ($\Delta\sigma_{os}$). The comparison between ($\Delta\sigma_{cs}$ + $\Delta\sigma_{ms}$) and $\Delta\sigma_{os}$ yielded a total $\Delta\sigma_p$ of 495 MPa for the secondary γ′ precipitates.

According to the literature[45], the tensile properties of materials are strongly influenced by their microstructures, particularly the morphology and distribution of precipitate particles. He et al. [46] enhanced the strength and ductility of alloys by controlling the formation and distribution of precipitate phases through the adjustment of Ti and Al additions and heat treatment conditions. They achieved a substantial precipitation strengthening contribution of 330.7 MPa, attributed to the formation of 22% γ' phase in the matrix and 3.6% Heusler phase at grain boundaries. Consistent with this mechanism, Wang et al. [47] successfully engineered a high density of $\mathrm{L1_2}$-structured γ′ precipitates in a $\mathrm{(CoFeNi)_{82}Ti_5Al_5V_8}$ alloy via thermomechanical processing (TMP). The precipitates achieved a volume fraction of 42%, with a corresponding precipitation strengthening contribution of 624 MPa. In contrast, Zhang et al. [48]developed an alloy featuring a face-centered cubic (fcc) high-entropy matrix and nano-sized γ′ particles. By generating precipitates of varying sizes in dendritic and interdendritic regions, with γ′ contents of 55% and 50%, respectively, they achieved a yield strength of 859 MPa and a precipitation strengthening contribution of 595 MPa.

Fig.8 presents a line graph illustrating the precipitation strengthening contributions of samples in various states. From the graph, it is evident that the precipitation strengthening contribution of specimens annealed at 1,025 ℃ and 1,050 ℃ is generally higher than that of specimens annealed at 1,075 ℃. Moreover, as the annealing time increases, the precipitation strengthening contribution gradually decreases. This phenomenon is attributed to the progressive dissolution of the secondary γ′ precipitates. Prior to reaching 1,075 ℃, although the size of the secondary γ′ precipitates does not change significantly with increasing annealing temperature, their volume fraction gradually diminishes, and they completely dissolve at 1,075 ℃. In nickel-based superalloys, when dislocations shear the ordered γ′ phase, the dislocations must appear in pairs to maintain the ordered structure. When paired dislocations cut through the γ′ phase, the conditions under which the dislocation pairs interact with the γ′ phase vary depending on the size of the γ′ phase [11]. The critical resolved shear stress (CRSS) required for two coupled edge dislocations to move along the [110] direction on the (111) plane of a single small-sized γ′ phase is lower than that for a large-sized γ′ phase[29]. Consequently, the gradual dissolution of the secondary γ′ precipitates leads to a progressive decline in the precipitation strengthening contribution, reaching its lowest value at 1,075 ℃.

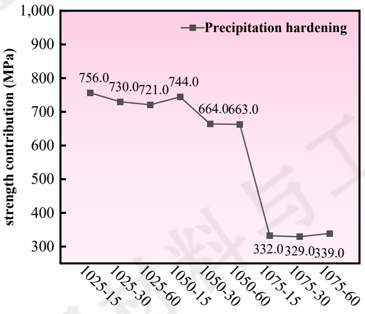

Fig.8 Line chart of precipitation strengthening contributions of samples in various states

4.1.3 Dislocation strengthening

In the cold rolling process, the plastic deformation of solid solution samples occurs through the continuous proliferation and interaction of dislocations under strain. Therefore, increasing the dislocation density will enhance the yield strength of the alloy. According to prior research, the strengthening effect is typically expressed as a function of dislocation density [49]:

$$\sigma_{\mathrm{d}} = \mathrm{M}\alpha\mathrm{Gb}\rho^{\frac{1}{2}} \tag{7}$$

where, M = 3 is the Taylor factor, α = 0.2 is the constant for FCC metals[50], G represents the shear modulus, which for this alloy is approximately 81.4 GPa at 293 K, b is the Burgers vector (for this alloy, 0.253 nm), and ρ is the geometrically necessary dislocation density. The geometrically necessary dislocation densities were primarily determined from EBSD analysis. The calculated GND densities were 5×10^{13} m^{-2} for the ST (solution-treated) specimen, 3.2×10^{14} m^{-2} for the 1025-15 specimen, 1.1×10^{14} m^{-2} for the 1050-15 specimen, and 9×10^{13} m^{-2} for the 1075-5 specimen. In calculating dislocation strengthening, since high-density dislocations originate from unrecrystallized grains rather than being related to recrystallized grains, it is necessary to multiply the dislocation strengthening by the proportion of unrecrystallized grains to obtain the true value of dislocation strengthening. This leads to the equation $\sigma_\mathrm{d} = M\alpha Gb\rho^{\frac{1}{2}} f_{UNRX}$, where f_{UNRX} is the fraction of grains that are not fully recrystallized. For ST, 1,025-15, 1,050-15 and 1,075-5 samples, the contribution of dislocation strengthening gradually decreases with the decrease of annealing temperature. The incompletely crystallized 1025-15 sample has the highest dislocation strengthening value of 60 MPa. In contrast, the dislocation strength increment of the samples annealed at 1050 °C and 1075 °C is almost zero, which is close to the level of the standard heat treatment samples.

Based on the above calculations, Fig.9 summarizes the contributions of four strengthening mechanisms in the nickel-cobalt-based high-temperature alloy under different conditions. It can be seen that the 1,025-15 and 1,050-15 samples are the two with the highest yield strength, representing the partially recrystallized and fully recrystallized states, respectively. Furthermore, the yield strength gradually decreases with prolonged annealing time. This is because, before reaching the critical temperature for strengthening mechanisms at 1,050 ℃, the yield strength is primarily contributed by grain boundary strengthening due to grain refinement and dislocation strengthening in the partially recrystallized state. As the annealing time increases, grain growth and the reduction in dislocation density result in a gradual decrease in yield strength. At 1,050 ℃, the primary contributions to yield strength are from grain boundary strengthening and precipitation strengthening. These effects are mainly due to changes in the size and distribution of precipitates, which increase the critical shear stress of dislocation pairs. With prolonged annealing time, grain growth and the dissolution of secondary γ' precipitates cause a gradual decrease in yield strength. At 1,075 ℃, beyond the critical threshold for this strengthening mechanism, the alloy's yield strength decreases significantly, primarily due to grain growth and the dissolution of secondary γ' precipitates.

4.2 Structures after tensile deformation

To investigate the tensile deformation mechanisms following thermomechanical processing, TEM analysis was conducted on samples in different conditions. Figs. 10(a_1-a_3) display the TEM images of the standard heat-treated (ST) sample. The sample comprises a γ matrix and γ' precipitates. SAED along the $[1\bar{1}2]$ zone axis reveals typical superlattice reflections of the FCC matrix (indicated by white circles) and the $L1_2$-structured γ' precipitates (highlighted by yellow circles), as shown in Fig. 10(a_1). A small number of secondary γ' precipitates and a large number of tertiary γ' precipitates are identified in the ST sample, surrounded by numerous dislocations, which form dislocation pile-ups and loops. Additionally, dislocations in the γ matrix can dissociate at the γ-γ' interfaces, leading to the formation of isolated stacking faults. High-resolution TEM (HRTEM) images reveal numerous isolated stacking faults (Fig. 10(a_3)), which expand continuously. Stacking faults with different orientations intersect at 70.5°, creating L-C locks, as shown in Fig. 10(a_1).

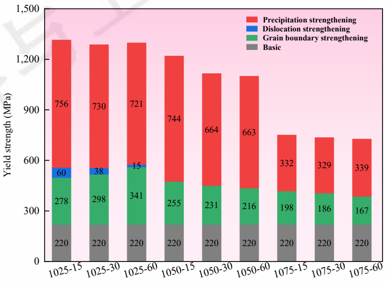

Fig. 9 Contributions of different strengthening mechanisms for samples in various states

Fig. 10(b_1-b_3) display the TEM images of the 1,025-15 sample. The microstructure comprises recrystallized grains (yellow regions) and deformed grains. The density of substructures in the deformed regions is higher than in the recrystallized regions. SAED along the [011] zone axis reveals typical superlattice reflections of the FCC matrix (indicated by white circles) and the $L1_2$-structured γ' precipitates (highlighted by yellow circles), as shown in Fig. 10(b1). High-resolution images reveal the presence of micro-nanotwins and dislocation pile-ups (Fig. 10(b_2)). Stacking faults with different orientations intersect at 70.5°, creating L-C locks, and dislocations pile up at the γ-γ' interfaces and grain boundaries, as shown in Fig. 10(b_3).

Figs. 10(c_1-c_3) present the TEM images of the 1050-15 sample. The microstructure is uniform, and SAED along the $[1\bar{1}2]$zone axis reveals typical superlattice reflections of the FCC matrix (indicated by white circles) and the $L1_2$-structured γ' precipitates (highlighted by yellow circles), as shown in Fig. 10(c_1). High-resolution images reveal the widespread presence of dense stacking faults and dislocations, with dislocation loops and stacking faults cutting into the precipitates (Fig. 10(c_2)). Stacking faults with different orientations intersect at 70.5°, creating L-C locks, and micro-nanotwins intersect with stacking faults, as shown in Fig. 8(c_3).

Regarding the superalloy studied in this paper, its yield strength and elongation have been compared and analyzed with the mechanical properties of some nickel-based/nickel-cobalt-based superalloys. As can be clearly observed from Figure 11,

稀有金属材料与工程

the alloy under our study occupies a very unique position in the property coordinate plot: the variation trend of its yield strength is similar to that of traditional superalloys—with the extension of hot working time and the increase of temperature, its strength decreases gradually, while its elongation is less affected by these factors. The results indicate that controlling the microstructure through appropriate thermomechanical processing is an effective strategy for achieving higher strength and ductility in nickel-cobalt-based high-temperature alloys.

4.3 Strain hardening rate

The strain hardening rates of the ST and various state samples are shown in Fig .12. It was found that when the strain is below the critical value, the strain hardening rates of all samples sharply decrease, corresponding to the elastic-plastic transition[51]. For the 1,025-15 sample, the strain hardening rate decreases to zero sooner after the elastic-plastic transition. This indicates that the severely deformed microstructure lacks sufficient strain hardening ability during plastic deformation, resulting in high yield strength but poor fracture elongation[52]. Compared to the standard heat-treated samples, all samples exhibit significant strain hardening rates. The strain hardening behavior of samples in different states is influenced by grain size[53]. When compared to the three hardening states exhibited by

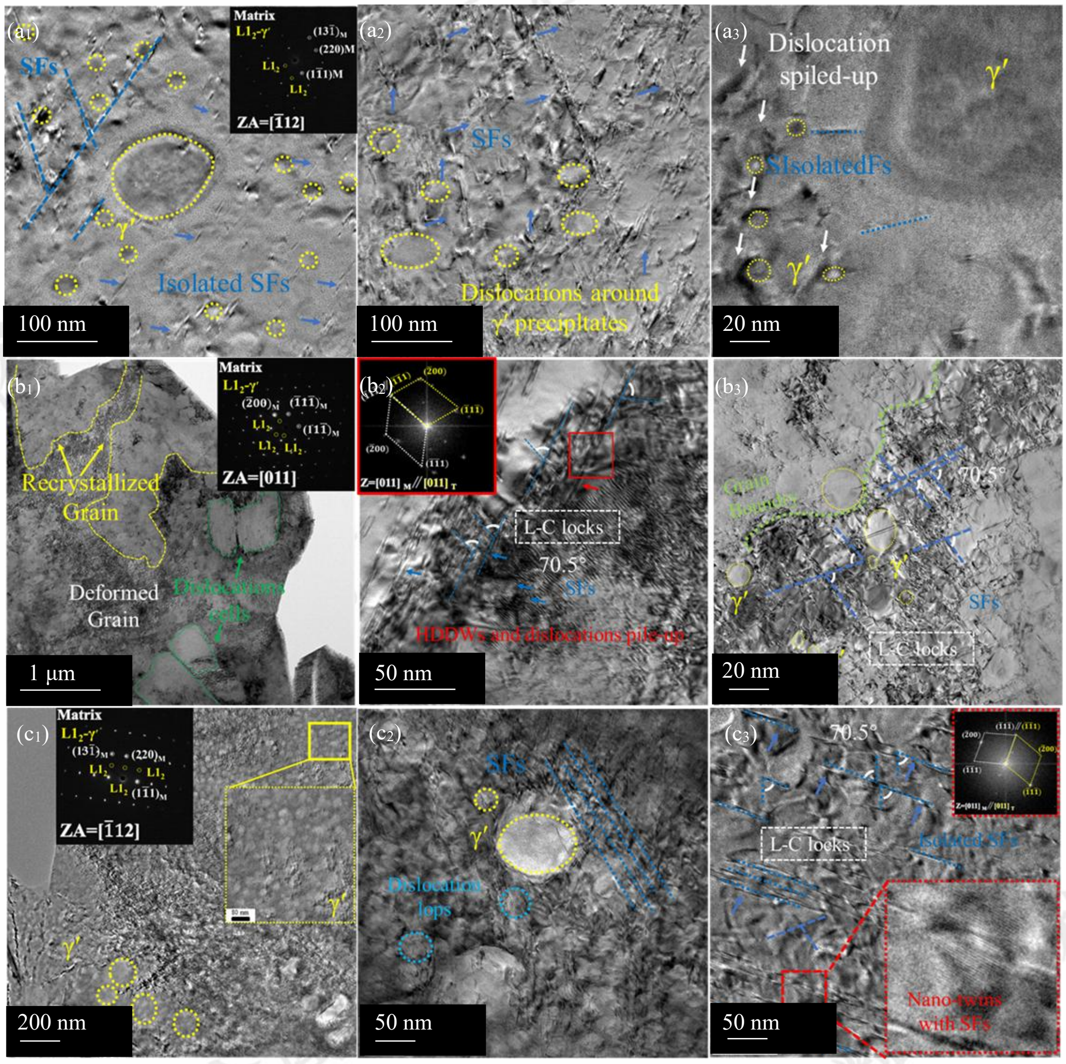

Fig. 10 TEM images of tensile fracture samples at room temperature: (a_1-a_3) ST; (b_1-b_3)1,025-15；(c_1-c_3)1,050-15

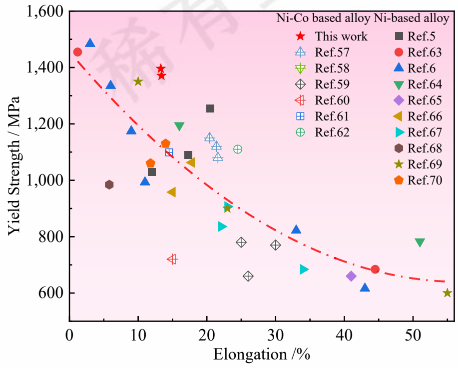

Fig.11 Comparison of the yield strength and elongation between the studied superalloy and some Ni-based and NiCo based superalloys [57-62,5,63,6,64-70]

coarse-grain (CG) samples, such as the 1,075-(15, 30, 60) sample, the hardening curves of fine-grain (FG) samples show an additional work-hardening region, i.e., the 1,025-(15, 30, 60) and 1,050-(10, 30, 60) samples. The FG samples show that region 2 begins with the increase in hardening rate. The transition from stage 1 to stage 2 corresponds to the initiation of twinning within the grains during multi-slip deformation, which is considered a necessary condition for twinning formation during plastic deformation[54,55]. The interaction between deformation twinning and dislocations can reduce stress concentration and contribute to an increased strain hardening rate[56].

4.3 Strain hardening rate

The strain hardening rates of the ST and various state samples are shown in Fig .12. It was found that when the strain is below the critical value, the strain hardening rates of all samples sharply decrease, corresponding to the elastic-plastic transition[51]. For the 1,025-15 sample, the strain hardening rate decreases to zero sooner after the elastic-plastic transition. This indicates that the severely deformed microstructure lacks sufficient strain hardening ability during plastic deformation, resulting in high yield strength but poor fracture elongation[52]. Compared to the standard heat-treated samples, all samples exhibit significant strain hardening rates. The strain hardening behavior of samples in different states is influenced by grain size[53]. When compared to the three hardening states exhibited by

coarse-grain (CG) samples, such as the 1,075-(15, 30, 60) sample, the hardening curves of fine-grain (FG) samples show an additional work-hardening region, i.e., the 1,025-(15, 30, 60) and 1,050-(10, 30, 60) samples. The FG samples show that region 2 begins with the increase in hardening rate. The transition from stage 1 to stage 2 corresponds to the initiation of twinning within the grains during multi-slip deformation, which is considered a necessary condition for twinning formation during plastic deformation[54,55]. The interaction between deformation twinning and dislocations can reduce stress concentration and contribute to an increased strain hardening rate[56].

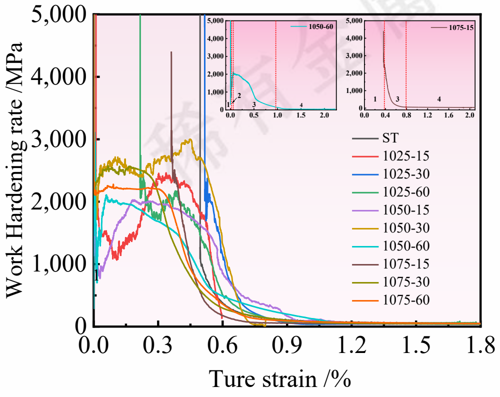

Fig.12 The relationship between the work-hardening rate and the true stress of specimens under different conditions

5 Conclusions

Although the standard heat-treated NiCo-based superalloy demonstrates excellent overall properties, its yield strength remains limited. In this study, an innovative method of multi-scale microstructure collaborative design through thermo-mechanical treatment has successfully broken through the obstacles of the traditional strength-plasticity inversion relationship and significantly improved the comprehensive properties of the alloy. Future work should prioritize investigating the strength evolution of specimens processed under varying hot deformation temperatures, thereby elucidating the influence of thermomechanical processing parameters on intermediate-temperature performance. The evolution of the microstructure before and after deformation was examined using EBSD and TEM. The key findings are summarized as follows:

1.The microstructural evolution of the Ni-Co-based superalloy after thermomechanical processing and aging treatments is strongly influenced by annealing temperature. Samples annealed at 1025 ℃ exhibit a partially recrystallized structure, comprising a γ matrix and three distinct γ′ precipitate populations. Fully recrystallized structures are observed in samples annealed at 1050 ℃, which retain the γ matrix and three γ′ precipitate populations. Notably, prolonged annealing at elevated temperatures induces progressive dissolution of secondary γ′ phases. Annealing at 1075 ℃ results in complete recrystallization, with the microstructure consisting of the γ matrix and two distinct γ′ precipitate size distributions.

2.Compared to standard heat treatment, the post-cold-rolling annealing process significantly enhances the yield strength of the alloy while concurrently reducing ductility. After annealing at 1025 ℃ for 15 minutes, the yield strength increases from 1,106 MPa to 1,371 MPa, with ductility decreasing from 18.8% to 13.3%. This strength enhancement originates from dislocation networks generated during cold rolling, grain refinement, and γ′ precipitate strengthening. Annealing at 1050 ℃ for 15 minutes further elevates the yield strength to 1,390 MPa, albeit with ductility reduced to 14.3%. The balanced strength-ductility synergy is attributed to the refined grain structure and γ′ precipitate distribution.

3.In NiCo-based superalloys subjected to standard heat treatment, the tensile deformation mechanism is governed by isolated stacking faults shearing through γ′ precipitates and dislocation-γ′ interactions, which promote dislocation pile-ups and the formation of dislocation cells. A limited number of intersecting stacking faults additionally form Lomer-Cottrell (L-C) locks. Thermomechanical processing (TMP) alters the deformation mechanism, inducing the formation of micro/nanoscale deformation twins. Furthermore, high-density L-C locks arise from intersecting stacking faults with varied orientations, while deformation twins propagate across these stacking faults. The synergistic strengthening-plasticizing effect is primarily attributed to these deformation twins, which enhance both

稀有金属材料与工程

strength and ductility by impeding dislocation motion while accommodating strain.

References

1 Reed Roger.*The Superalloys: Fundamentals and Applications*[J], 2006: 1-372

2 H. Wen, S. Wang, J. Jin, X. Wang et al. Journal of Materials Processing Technol.[J], 2024, 324: 118226.

3 H. Wen, J. Jin, X. Tang, X et al. Journal of Materials Science & Technology[J], 2023, 162: 57-73.

4 Yang C L, Zhang Z J, Zhang P *et al.Materials Science and Engineering A*[J], 2018, 736: 100-104

5 Zhao Yanan, Ma Zongqing, Yu Liming *et al.Journal of Materials Science and Technology*[J], 2021, 68: 184-190

6 Polkowska Adelajda, Lech Sebastian, Polkowski Wojciech.*Materials Science and Engineering: A*[J], 2020, 787: 139478

7 Heckl A, Neumeier S, Göken M *et al.Materials Science and Engineering: A*[J], 2011, 528(9): 3435-3444

8 Gypen L A, Deruyttere A.*Journal of Materials Science*[J], 1977, 12(5): 1034-1038

9 Takizawa Yoichi, Otsuka Kenshi, Masuda Takahiro *et al.Materials Science and Engineering: A*[J], 2015, 648: 178-182

10 Chen Ming Song, Zou Zong Huai, Lin Y C *et al.Materials Characterization*[J], 2019, 151: 445-456

11 Zhu C Z, Zhang R, Cui C Y *et al.Materials Science and Engineering: A*[J], 2021, 802: 140646

12 Li Weiguo, Ma Jianzuo, Kou Haibo et al.*International Journal of Plasticity*[J], 2019, 116: 143-158

13 Kozar R W, Suzuki A, Milligan W W *et al.Metallurgical and Materials Transactions A*[J], 2009, 40(7): 1588-1603

14 Benyoucef M, Coujou A, Barbker B *et al.Materials Science and Engineering: A*[J], 1997, 234-236: 692-694

15 Song Xiaoqing, Wang Yongxin, Zhang Jing *et al.Materials Science and Engineering: A*[J], 2021, 806: 140820

16 Lu Song, Antonov Stoichko, Li Longfei *et al.Acta Materialia*[J], 2020, 190: 16-28

17 Li Xiuyan, Lu K.*Science*[J], 2019, 364(6442): 733-734

18 Li Xiuyan, Lu K.*Nature Materials*[J], 2017, 16(7): 700-701

19 Oliveira J P, Curado T M, Zeng Z *et al.Materials & Design*[J], 2020, 189: 108505

20 Langdon Terence G.*Acta Materialia*[J], 2013, 61(19): 7035-7059

21 Chen G, Qiao J W, Jiao Z M *et al.Scripta Materialia*[J], 2019, 167: 95-100

22 Wang Changshuai, Guo Yongan, Guo Jianting *et al.Materials Science and Engineering A*[J], 2016, 675: 314-322

23 Singh M, Jonnalagadda K N.*Experimental Mechanics*[J], 2024, 64(5): 703-727

24 Gu Ji, Guo Lin, Gan Bin *et al.Materials Science and Engineering A*[J], 2021, 802: 140676

25 Zeng M T, Yang Y, Tan Y B *et al.Materials Characterization*[J], 2023, 197: 112656

26 Wang Dian, Pei Biao, Wang Zhong *et al.Intermetallics*[J], 2023, 155: 107836

27 Chen Guidong, Liu Fei, Chen Fei *et al.Materials Science and Engineering A*[J], 2024, 904: 146687

28 Zhang Zijiao, Sheng Hongwei, Wang Zhangjie *et al.Nature Communications*[J], 2017, 8(1): 14390

29 Shih Mulaine, Miao Jiashi, Mills Michael *et al.Nature Communications*[J], 2021, 12(1): 3590

30 Schwarze Christian, Darvishi Kamachali Reza, Steinbach Ingo.*Acta Materialia*[J], 2016, 106: 59-65

31 Wang Zhenfan, Ren Xiaona, Wang Yao *et al.Materials Science and Engineering A*[J], 2024, 913: 147011

32 Cui Luqing, Yu Jinjiang, Liu Jinlai *et al.Materials Science and Engineering A*[J], 2018, 710: 309-317

33 Azarbarmas M, Aghaie-Khafri M, Cabrera J M *et al.Materials & Design*[J], 2016, 94: 28-38

34 Wendt H, Haasen P.*Acta Metallurgica*[J], 1983, 31(10): 1649-1659

35 Li Hualong, Hsu Emilie, Szpunar Jerzy *et al.Journal of Materials Science*[J], 2008, 43(22): 7148-7156

36 Li Y, Bushby A J, Dunstan D J.*Proceedings of the Royal Society A: Mathematical, Physical and Engineering Sciences*[J], 2016, 472(2190): 20150890

37 Hall E O.*Proceedings of the Physical Society. Section B*[J], 1951, 64(9): 747

38 Wang chen, Wang Xingmao.*Rare Metal Materials and Engineering*[J], 2024, 53(1): 113-123

39 Zhao Y Y, Chen H W, Lu Z P *et al.Acta Materialia*[J], 2018, 147: 184-194

40 Ma Kaka, Wen Haiming, Hu Tao *et al.Acta Materialia*[J], 2014, 62: 141-155

41 Wen Haiming, Topping Troy D, Isheim Dieter *et al.Acta Materialia*[J], 2013, 61(8): 2769-2782

42 He J Y, Wang H, Huang H L *et al.Acta Materialia*[J], 2016, 102: 187-196

43 Ardell A J.*Metallurgical Transactions A*[J], 1985, 16(12): 2131-

稀有金属材料与工程

2165

44 Yasuda H, Takasugi T, Koiwa M.*Acta Metallurgica et Materialia*[J], 1992, 40(2): 381-387

45 Duan Jixuan, An Teng, Gu Yu *et al.Materials Science and Engineering A*[J], 2023, 865: 144323

46 He J Y, Wang H, Wu Y *et al.Intermetallics*[J], 2016, 79: 41-52

47 Wang Lei, Kong Lingming, Li Yixin *et al.Materials Science and Engineering A*[J], 2024, 893: 146138

48 Zhang Lu, Zhou Yang, Jin Xi *et al.Materials Science and Engineering A*[J], 2018, 732: 186-191

49 Mecking H, Kocks U F.*Acta Metallurgica*[J], 1981, 29(11): 1865-1875

50 Zhang B B, Yan F K, Zhao M J *et al.Acta Materialia*[J], 2018, 151: 310-320

51 Yan F K, Liu G Z, Tao N R *et al.Acta Materialia*[J], 2012, 60(3): 1059-1071

52 Zhu Yuntian T, Liao Xiaozhou.*Nature Materials*[J], 2004, 3(6): 351-352

53 Rahman K M, Vorontsov V A, Dye D.*Acta Materialia*[J], 2015, 89: 247-257[J]

54 Rémy L.*Acta Metallurgica*[J], 1977, 25(6): 711-714

55 Rémy L.*Metallurgical Transactions A*[J], 1981, 12(3): 387-408

56 Niu Gang, Tang Qibo, Wu Huibin *et al.Materialia*[J], 2019, 6: 100264

57 Slone C E, Miao J, Mills M J.*Scripta Materialia*[J], 2018, 155: 94-98

58 Zhu C Z, Zhang R, Cui C Y *et al.Metallurgical and Materials Transactions A*[J], 2021, 52(1): 108-118

59 Xu H, Zhang Z J, Zhang P *et al.Scientific Reports*[J], 2017, 7(1): 8046

60 Bian Huakang, Cui Yujie, Li Yunping *et al.Journal of Alloys and Compounds*[J], 2018, 768: 136-142

61 Yuan Y, Gu Y F, Zhong Z H *et al.Materials Science and Engineering A*[J], 2012, 556: 595-600

62 Wang Xingmao, Ding Yutian, Yu Hongyao *et al.Materials Science and Engineering A*[J], 2022, 847: 143293

63 Sun Yan Le, Fu Li Ming, Lv Li Feng *et al.Materials Science Forum*[J], 2016, 848: 588-592

64 Wang Xingmao, Ding Yutian, Gao Yubi *et al.Materials Science and Engineering: A*[J], 2021, 823: 141739

65 Praveen K V U, Sastry G V S, Singh Vakil.*Metallurgical and Materials Transactions A*[J], 2008, 39(1): 65-78

66 Hosseini Seyed Ali, Abbasi Seyed Mehdi, Madar Karim Zangeneh.*Materials Science and Engineering A*[J], 2018, 712: 780-789

67 Polkowski Wojciech, Polkowska Adelajda, Lech Sebastian.*Journal of Alloys and Compounds*[J], 2021, 860: 158418

68 Zhang P, Yuan Y, Shi X B *et al.Metallurgical and Materials Transactions a*[J], 2021, 52(9): 3699-3705

69 Morakabati Maryam, Ahmadian Peyman, Goodarzi Mohammad Rasoul Moazami.*Metallurgical Research & Technology*[J], 2020, 117(4)

70 Harte Allan, Atkinson Michael, Smith Albert *et al.Acta Materialia*[J], 2020, 194: 257-275

热机械加工对 NiCo 基高温合金微观组织和力学性能的影响

高明 [1]，张倩 [1]，乔珺威 [1,2]，甘斌 [3]

(1. 太原理工大学材料科学与工程学院，山西 太原 030024)

(2. 太原理工大学先进材料界面科学与工程教育部重点实验室，山西 太原 030024)

(3. 苏州实验室，中国苏州市若水街道 388 号，江苏 215123)

摘　要：高效实现优异的强塑协同效应是先进结构材料的核心研发目标。本研究通过短时退火与时效处理，在镍钴基高温合金中构建出一种新型晶粒结构 —— 该结构包含残余变形晶粒、细小再结晶晶粒及多尺度 $L1_2$-γ′析出相。与传统热处理态合金（屈服强度：1106 MPa；延伸率：18.8%）相比，具有部分再结晶显微组织的合金屈服强度显著提升至 1371 MPa，同时保持了 13.3% 的延伸率。这一高强度特性源于位错强化（由前期冷轧引入）、细晶强化与 γ′相沉淀强化的协同作用。与之相对，完全再结晶态合金的屈服强度为 1390 MPa、延伸率为 14.3%，其性能优势主要得益于均匀的细晶组织与弥散分布的 γ′析出相。研究还深入探究了材料的内在变形机制，结果表明：除析出相外，位错运动、纳米孪晶及 L-C 位错锁（L-C locks）对合金卓越力学性能的实现也起到关键作用。本研究为研发面向严苛工程应用的高性能镍钴基高温合金，提供了一种实用且成本效益高的加工策略。

关键词：镍钴基高温合金；热机械处理；强塑性匹配； $L1_2$-γ′相析出；组织演变

稀有金属材料与工程

作者简介：高　明，男，2000 年生，硕士生，太原理工大学材料科学与工程学院，山西　太原　030024，E-mail: g1193629573@163.com

稀有金属材料与工程
稀有金属材料与工程
稀有金属材料与工程
稀有金属材料与工程